Mon. Not. R. Astron. Soc. **000**, 1–14 (0000) Printed 13 July 2016 (MN LaTeX style file v2.2)

The clustering of galaxies in the completed SDSS-III Baryon Oscillation Spectroscopic Survey: tomographic BAO analysis of DR12 combined sample in configuration space

Yuting Wang[1,2]⋆, Gong-Bo Zhao[1,2]†, Chia-Hsun Chuang[3,4], Ashley J. Ross[5], Will J. Percival[2], Héctor Gil-Marín[2], Antonio J. Cuesta[6], Francisco-Shu Kitaura[4], Sergio Rodriguez-Torres[3,7,8], Joel R. Brownstein[9], Daniel J. Eisenstein[10], Shirley Ho[11,12,13], Jean-Paul Kneib[14], Matt Olmstead[15], Francisco Prada[7], Graziano Rossi[16], Ariel G. Sánchez[17], Salvador Salazar-Albornoz[18,17], Daniel Thomas[2], Jeremy Tinker[19], Rita Tojeiro[20], Mariana Vargas-Magaña[21], Fangzhou Zhu[22]

[1] *National Astronomy Observatories, Chinese Academy of Science, Beijing, 100012, P. R. China*
[2] *Institute of Cosmology & Gravitation, University of Portsmouth, Dennis Sciama Building, Portsmouth, PO1 3FX, UK*
[3] *Instituto de Física Teórica, (UAM/CSIC), Universidad Autónoma de Madrid, Cantoblanco, E-28049 Madrid, Spain*
[4] *Leibniz-Institut für Astrophysik Potsdam (AIP), An der Sternwarte 16, 14482 Potsdam, Germany*
[5] *Center for Cosmology and AstroParticle Physics, The Ohio State University, Columbus, OH 43210, USA*
[6] *Institut de Ciències del Cosmos (ICCUB), Universitat de Barcelona (IEEC- UB), Martí i Franquès 1, E-08028 Barcelona, Spain*
[7] *Campus of International Excellence UAM+CSIC, Cantoblanco, E-28049 Madrid, Spain*
[8] *Departamento de Física Teórica, Universidad Autónoma de Madrid, Cantoblanco, E-28049, Madrid, Spain*
[9] *Department of Physics and Astronomy, University of Utah, 115 S 1400 E, Salt Lake City, UT 84112, USA*
[10] *Harvard-Smithsonian Center for Astrophysics, 60 Garden St., Cambridge, MA 02138, USA*
[11] *McWilliams Center for Cosmology, Department of Physics, Carnegie Mellon University, 5000 Forbes Ave., Pittsburgh, PA 15213*
[12] *Lawrence Berkeley National Laboratory, 1 Cyclotron Rd, Berkeley, CA 94720*
[13] *Department of Physics, University of California, Berkeley, CA 94720*
[14] *Laboratoire d'Astrophysique, Ecole Polytechnique Fédérale de Lausanne (EPFL), Observatoire de Sauverny, CH-1290 Versoix, Switzerland*
[15] *Department of Chemistry and Physics, King's College, 133 North River St, Wilkes Barre, PA 18711, USA*
[16] *Department of Astronomy and Space Science, Sejong University, Seoul 143-747, Korea*
[17] *Max-Planck-Institut für extraterrestrische Physik, Postfach 1312, Giessenbachstr., 85741 Garching, Germany*
[18] *Universität Sternwarte Muänchen, Ludwig Maximilian Universität, Munich, Germany*
[19] *Center for Cosmology and Particle Physics, Department of Physics, New York University, 4 Washington Place, New York, NY 10003, USA*
[20] *School of Physics and Astronomy, University of St Andrews, North Haugh, St Andrews KY16 9SS, UK*
[21] *Instituto de Fisica, Universidad Nacional Autonoma de Mexico, Apdo. Postal 20-364, Mexico*
[22] *Department of Physics, Yale University, New Haven, CT 06511, USA*

13 July 2016

ABSTRACT

We perform a tomographic baryon acoustic oscillations analysis using the two-point galaxy correlation function measured from the combined sample of BOSS DR12, which covers the redshift range of $0.2 < z < 0.75$. Splitting the sample into multiple overlapping redshift slices to extract the redshift information of galaxy clustering, we obtain a measurement of $D_A(z)/r_d$ and $H(z)r_d$ at nine effective redshifts with the full covariance matrix calibrated using MultiDark-Patchy mock catalogues. Using the reconstructed galaxy catalogues, we obtain the precision of $1.3\% - 2.3\%$ for $D_A(z)/r_d$ and $2.5\% - 5.7\%$ for $H(z)r_d$. To quantify the gain from the tomographic information, we compare the constraints on the cosmological parameters using our 9-bin BAO measurements, the consensus 3-bin BAO and RSD measurements at three effective redshifts in Alam (2016), and the non-tomographic (1-bin) BAO measurement at a single effective redshift. Comparing the 9-bin with 1-bin constraint result, it can improve the dark energy Figure of Merit by a factor of 1.35 for the Chevallier-Polarski-Linder parametrisation for equation of state parameter $w_{\rm DE}$. The errors of w_0 and w_a from 9-bin constraints are slightly improved by 4% when compared to the 3-bin constraint result.

Key words:
baryon acoustic oscillations, distance scale, dark energy

1 INTRODUCTION

The accelerating expansion of the Universe was discovered by the observation of type Ia supernovae (Riess et al. 1998; Perlmutter et al. 1999). Understanding the physics of the cosmic acceleration is one of the major challenges in cosmology. In the framework of general relatively (GR), a new energy component with a negative pressure, dubbed dark energy (DE), can be the source driving the cosmic acceleration. Observations reveal that the DE component dominates the current Universe (Weinberg et al. 2013). However, the nature of DE remains unknown. Large cosmological surveys, especially for galaxy redshift surveys, can provide key observational support for the study of DE.

Galaxy redshift surveys are used to map the large scale structure of the Universe, and extract the signal of baryon acoustic oscillation (BAO). The BAO, produced by the competition between gravity and radiation due to the couplings between baryons and photons before the cosmic recombination, leave an imprint on the distribution of galaxies at late times. After the photons decouple, the acoustic oscillations are frozen and correspond to a characteristic scale, determined by the comoving sound horizon at the drag epoch, $r_d \sim 150\,{\rm Mpc}$. This feature corresponds to an excess on the 2-point correlation function, or a series of wiggles on the power spectrum. The acoustic scale is regarded as a standard ruler to measure the cosmic expansion history, and to constrain cosmological parameters (Eisenstein et al. 2005). If assuming an isotropic galaxies clustering, the combined volume distance, $D_V(z) \equiv \left[cz(1+z)^2 D_A(z)^2 H^{-1}(z)\right]^{1/3}$, where $H(z)$ is the Hubble parameter and $D_A(z)$ is the angular diameter distance, can be measured using the angle-averaged 2-point correlation function, $\xi_0(s)$ (Eisenstein et al. 2005; Kazin et al. 2010; Beutler et al. 2011; Blake et al. 2011) or power spectrum $P_0(k)$ (Tegmark et al. 2006; Percival et al. 2007; Reid et al. 2010). However, in principle the clustering of galaxies is anisotropic, the BAO scale can be measured in the radial and transverse directions to provide the Hubble parameter, $H(z)$, and angular diameter distance, $D_A(z)$, respectively. As proposed by Padmanabhan & White 2008, the "multipole" projection of the full 2D measurement of power spectrum, $P_\ell(k)$, were used to break the degeneracy of $H(z)$ and $D_A(z)$. This multipole method was applied into the correlation function (Chuang & Wang 2012, 2013; Xu et al. 2013). Alternative "wedge" projection of correlation function, $\xi_{\Delta\mu}(s)$, was used to constrain parameters, $H(z)$ and $D_A(z)$ (Kazin et al. 2012, 2013). In Anderson et al. (2014), the anisotropic BAO analysis was performed using these two projections of correlation function from SDSS-III Baryon Oscillation Spectroscopic Survey (BOSS) DR10 and DR11 samples.

The BOSS (Dawson et al. 2013), which is part of SDSS-III (Eisenstein et al. 2011), has provided the Data Release 12 (Alam et al. 2015). With a redshift cut, the whole samples are split into the 'low-redshift' samples (LOWZ) in the redshift range $0.15 < z < 0.43$ and 'constant stellar mass' samples (CMASS) in the redshift range $0.43 < z < 0.7$. Using these catalogues, the BAO peak position was measured at two effective redshifts, $z_{\rm eff} = 0.32$ and $z_{\rm eff} = 0.57$, in the multipoles of correlation function (Cuesta et al. 2016) or power spectrum (Gil-Marín et al. 2015). Chuang 2016 proposed to divide each sample of LOWZ and CMASS into two independent redshift bins, thus to test the extraction of redshift information from galaxy clustering. They performed the measurements on BAO and growth rate at four effective redshifts, $z_{\rm eff} = 0.24,\ 0.37,\ 0.49$ and 0.64 (Chuang 2016).

The completed data release of BOSS will provide a combined sample, covering the redshift range from 0.2 to 0.75. The sample is divided into three redshift bins, *i.e.*, two independent redshift bins, $0.2 < z < 0.5$ and $0.5 < z < 0.75$, and an overlapping redshift bin, $0.4 < z < 0.6$. The BAO signal is measured at the three effective redshifts, $z_{\rm eff} = 0.38,\ 0.51$ and 0.61 using the configuration-space correlation function (Ross 2016; Vargas-Magaña et al. 2016) or Fourier-space power spectrum (Beutler 2016a).

As the tomographic information of galaxy clustering is important to constrain the property of DE (Salazar-Albornoz et al. 2014; Zhao 2016a), we will extract the information of redshift evolution from the combined catalogue as much as possible. To achieve this, we adopt the binning method. The binning scheme is determined through the forecasting result using Fisher matrix method. We split

⋆ Email: ytwang@nao.cas.cn
† Email: gbzhao@nao.cas.cn

the whole sample into *nine overlapping* redshift bins to make sure that the measurement precision of the isotropic BAO signal is better than 3% in each bin. We perform the measurements on the an/isotropic BAO positions in the *nine overlapping* bins using the correlation functions of the pre- and post-reconstruction catalogues. To test the constraining power of our tomographic BAO measurements, we perform the fitting of cosmological parameters.

The analysis is part of a series of papers analysing the clustering of the completed BOSS DR12 (Alam 2016; Zhao 2016b; Beutler 2016a,b; Ross 2016; Sánchez 2016a,b; Salazar-Albornoz 2016; Vargas-Magaña et al. 2016; Grieb 2016; Chuang 2016; Pellejero-Ibanez 2016). The same tomographic BAO analysis is performed using galaxy power spectrum in Fourier space (Zhao 2016b). Another tomographic analysis is performed using the angular correlation function in many thin redshift shells and their angular cross-correlations in the companion paper, Salazar-Albornoz (2016), to extract the time evolution of the clustering signal.

In Section 2, we introduce the data and mocks used in this paper. We present the forecast result in Section 3. In Section 4, we describe the methodology to measure the BAO signal using multipoles of correlation function. In Section 5, we constrain cosmological models using the BAO measurement from the post-reconstructed catalogues. Section 6 is devoted to the conclusion. In this paper, we use a fiducial ΛCDM cosmology with the parameters: $\Omega_m = 0.307, \Omega_b h^2 = 0.022, h = 0.6777, n_s = 0.96, \sigma_8 = 0.8288$. The comoving sound horizon in this cosmology is $r_d^{\rm fid} = 147.74\,\mathrm{Mpc}$.

2 DATA AND MOCKS

We use the completed catalogue of BOSS DR12, which covers the redshift range from 0.2 to 0.75. In the North Galactic Cap (NGC), $864,923$ galaxies over the effective coverage area of $5923.90\,\mathrm{deg}^2$ are observed and the South Galactic Cap (SGC) contains $333,081$ with the effective coverage area of $2517.65\,\mathrm{deg}^2$. The volume density distribution from observation is shown in solid curves of Figure 1.

In oder to correct for observational effects, the catalogue is given a set of weights, including weights for the redshift failure, $w_{\rm zf}$, close pair due to fiber collisions, $w_{\rm cp}$ and for systematics, $w_{\rm sys}$. In addition, the FKP weight to achieve a balance between the regions of high density and low density (Feldman et al. 1994) is added

$$w_{\rm FKP} = \frac{1}{1 + n(z) P_0}, \tag{1}$$

where $n(z)$ is the number density of galaxies, and P_0 is set to $10,000\,h^{-3}\mathrm{Mpc}^3$. Thus each galaxy is counted by adding a total weight as below

$$w_{\rm tot} = w_{\rm FKP} w_{\rm sys} (w_{\rm cp} + w_{\rm zf} - 1). \tag{2}$$

The details about the observational systematic weights are described in Ross (2016).

The correlation function is measured by comparing the galaxy distribution to a randomly distributed catalogue, which is reconstructed with the same radial selection function as the real catalogue, but without clustering structure. We use a random catalogue consisting of 50 times random galaxies of the observed sample.

During the cosmic evolution, non-linear structure formation and redshift space distortions (RSD) can weaken the significance of the BAO peak thus degrade the precision of BAO measurements. The BAO signal can be boosted to some extent by the reconstruction procedure, which effectively moves the galaxies to the positions as if there was no RSD and nonlinear effects (Eisenstein et al. 2007a). We will also present BAO measurements using the catalogue, which is reconstructed through the reconstruction algorithm as described in Padmanabhan et al. (2012).

Mock galaxy catalogues are required to determine the data covariance matrix, and to test the methodology. We use the MultiDark-Patchy mock catalogues (Kitaura et al. 2016). The mock catalogues are constructed to match the observed data on the angular selection function, redshift distribution, and clustering statistics (*e.g.* 2-point and 3-point correlation functions). We utilise 2045 mock catalogues for the pre-reconstruction, and 1000 mocks for the post-reconstruction. We perform the measurement for each mock catalogue, then estimate the covariance matrix of data correlation function using the method proposed in Percival et al. (2014).

3 BAO FORECASTS

We first determine the binning scheme through the Fisher matrix method. We use the Fisher matrix formulism in (Tegmark 1997; Seo & Eisenstein 2007) to predict the BAO distance parameters. Starting with the galaxy power spectrum, $P(k,\mu)$, the fisher matrix is

$$F_{ij} = \int_{-1}^{1} \int_{k_{\rm min}}^{k_{\rm max}} \frac{\partial \ln P(k,\mu)}{\partial p_i} \frac{\partial \ln P(k,\mu)}{\partial p_j} V_{\rm eff}(k,\mu) \frac{k^2 dk d\mu}{8\pi^2}, \tag{3}$$

here we set $k_{\rm min} = 2\pi / V_{\rm sur}^{1/3}\,h\,\mathrm{Mpc}^{-1}$ and $k_{\rm max} = 0.3\,h\,\mathrm{Mpc}^{-1}$.

In order to ensure that the isotropic BAO measurement precision in each bin is better than 3%, we split the whole redshift range, *i.e.* $[0.2, 0.75]$ into 9 overlapping bins. The width of the first and last bins is 0.19, and other bins have the same bin width, *i.e.* $\Delta z = 0.15$.

In Table 1, we present the 9 overlapping redshift ranges, the effective redshifts and numbers of the samples in the NGC and SGC. In Figure 1, the overlapping histograms denote the average number density in each bin.

Combining the results of NGC and SGC samples as,

$$F_{ij}^{\rm NGC+SGC} = F_{ij}^{\rm NGC} + F_{ij}^{\rm SGC}, \tag{4}$$

we present the forecast result on the precision of the BAO distance parameters, including the angular diameter distance $D_A(z)$, Hubble parameter $H(z)$ and volume distance $D_V(z)$ in Table 2. It is seen that the isotropic BAO prediction in each bin can reach, $\sigma_{D_V}/D_V < 3\%$. With the "50%" reconstructed efficiency, which means that the nonlinear damping scales, $\Sigma_\perp$ and $\Sigma_\parallel$, are reduced by a factor 0.5 and there is the remaining 50% nonlinearity, the isotropic BAO precision is within $0.8\% - 1.2\%$.

The predictions on the precision of anisotropic BAO parameters are within $1.8\% - 2.9\%$ for the angular diameter distance and $4.2\% - 7.1\%$ for the Hubble parameter without the reconstruction. Considering the "50%" reconstruction, the best prediction can reach 1.1% for $D_A(z)$ and 2.1% for $H(z)$. The contour plot of $D_A(z)$ and $H(z)$ within $2\,\sigma$ error is displayed in Figure 2, where the black points are the fiducial values. The left panel in Figure 2 shows the forecast result without reconstruction, and the right panel presents the "50%" reconstructed result.

z bins	$z_{\rm eff}$	NGC	SGC
$0.20 < z < 0.39$	0.31	208517	89242
$0.28 < z < 0.43$	0.36	194754	81539
$0.32 < z < 0.47$	0.40	230388	93825
$0.36 < z < 0.51$	0.44	294749	115029
$0.40 < z < 0.55$	0.48	370429	136117
$0.44 < z < 0.59$	0.52	423716	154486
$0.48 < z < 0.63$	0.56	410324	149364
$0.52 < z < 0.67$	0.59	331067	121145
$0.56 < z < 0.75$	0.64	243763	91170

Table 1. The 9 overlapping redshift bins, the effective redshift and the number of samples in each bin.

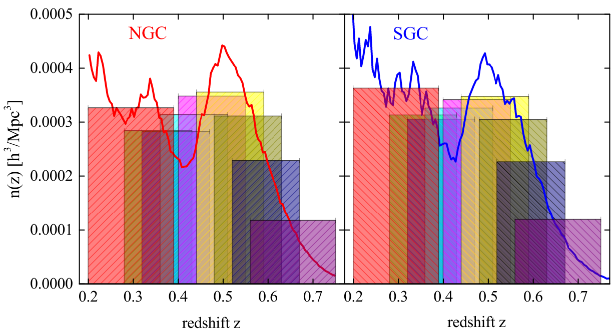

Figure 1. The overlapping histograms in different colours are the average number densities in 9 redshift bins, which is used to do the forecasts. The solid lines are the number densities for the NGC/SGC samples.

4 BAO MEASUREMENTS

4.1 The estimator for the 2-pt correlation function

We measure the correlation function of the combined sample using the Landy & Szalay (1993) estimator:

$$\xi(s,\mu) = \frac{DD(s,\mu) - 2DR(s,\mu) + RR(s,\mu)}{RR(s,\mu)}, \quad (5)$$

where DD, DR and RR are the weighted data-data pair counts, data-random pair counts and random-random pair counts with the separation, s and the cosine of the angle of the pair to the line of sight, μ.

Table 2. The forecast results on the BAO distance parameters without reconstruction (and "50%" reconstruction) using the combination of NGC and SGC samples.

$z_{\rm eff}$	σ_{D_A}/D_A	σ_H/H	σ_{D_V}/D_V
0.31	0.0289 (159)	0.0705 (309)	0.0236 (114)
0.36	0.0281 (159)	0.0681 (307)	0.0229 (113)
0.40	0.0254 (145)	0.0616 (281)	0.0207 (104)
0.44	0.0226 (130)	0.0553 (253)	0.0185 (093)
0.48	0.0203 (118)	0.0502 (230)	0.0167 (085)
0.52	0.0188 (110)	0.0464 (214)	0.0155 (079)
0.56	0.0180 (108)	0.0441 (208)	0.0147 (077)
0.59	0.0183 (113)	0.0436 (214)	0.0147 (080)
0.64	0.0187 (122)	0.0418 (222)	0.0144 (085)

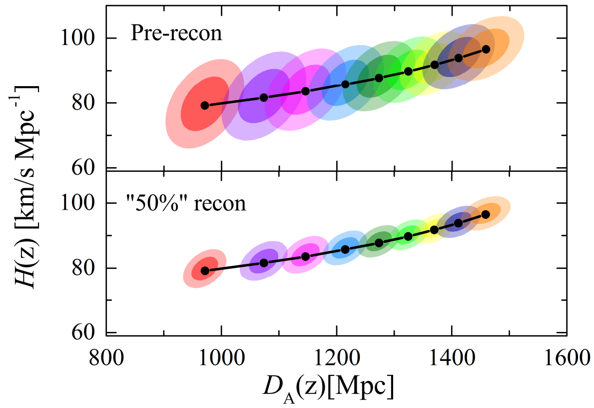

Figure 2. The 68 and 95% CL contour plots of the transverse and radial distance parameters, $D_A(z)$ and $H(z)$, in 9 redshift bins are shown one by one from left to right. The left panel shows the result without the reconstruction, and the right panel is the result with "50%" reconstructed efficiency.

The multipole projections of the correlation function can be calculated through

$$\xi_l(s) = \frac{2l+1}{2}\int_{-1}^{1} {\rm d}\mu\, \xi(s,\mu)\mathcal{L}_\ell(\mu), \quad (6)$$

where $\mathcal{L}_\ell(\mu)$ is the Legendre Polynomial.

We also measure the correlation function of the reconstructed catalogue using the Landy & Szalay (1993) estimator:

$$\xi(s,\mu) = \frac{DD(s,\mu) - 2DS(s,\mu) + SS(s,\mu)}{RR(s,\mu)}, \quad (7)$$

here we used the shifted data and randoms for DD, DS, and SS.

The measured monopole and quadruple of correlation function from data and mocks in each redshift bin are shown in Figure 3, where the blue squares with $1\,\sigma$ error bar are the data measurements before reconstruction, and the blue shaded regions are the standard deviation from the pre-reconstructed mocks around the average. The red points with $1\,\sigma$ error bar are the data measurements after reconstruction, and the red shaded regions denote the average with a standard deviation from the post-reconstructed mocks. The 2D correlation functions in 9 redshift bins are plotted in Figure 4, where the BAO ring in each redshift slice is visualised.

4.2 The template

The isotropic BAO position is parameterised by the scale dilation parameter,

$$\alpha \equiv \frac{D_V(z) r_{d,{\rm fid}}}{D_V^{\rm fid}(z) r_d} \, . \quad (8)$$

We adopt the template for the correlation function in the isotropic case (Eisenstein et al. 2007b),

$$\xi^{\rm mod}(s) = \int \frac{k^2 dk}{2\pi^2} P_{\rm dw}^{\rm mod}(k) j_0(ks) e^{-k^2 a^2} \, , \quad (9)$$

where the Gaussian term is introduced to damp the oscillations from $j_0(ks)$, and here we set $a = 1\,h^{-1}\,{\rm Mpc}$. The de-wiggled power spectrum, $P_{\rm dw}^{\rm mod}(k)$, is given by

$$P_{\rm dw}^{\rm mod}(k) = P^{\rm nw}(k) + \left[P^{\rm lin}(k) - P^{\rm nw}(k)\right] e^{-\frac{1}{2}k^2\Sigma_{nl}^2} \, , \quad (10)$$

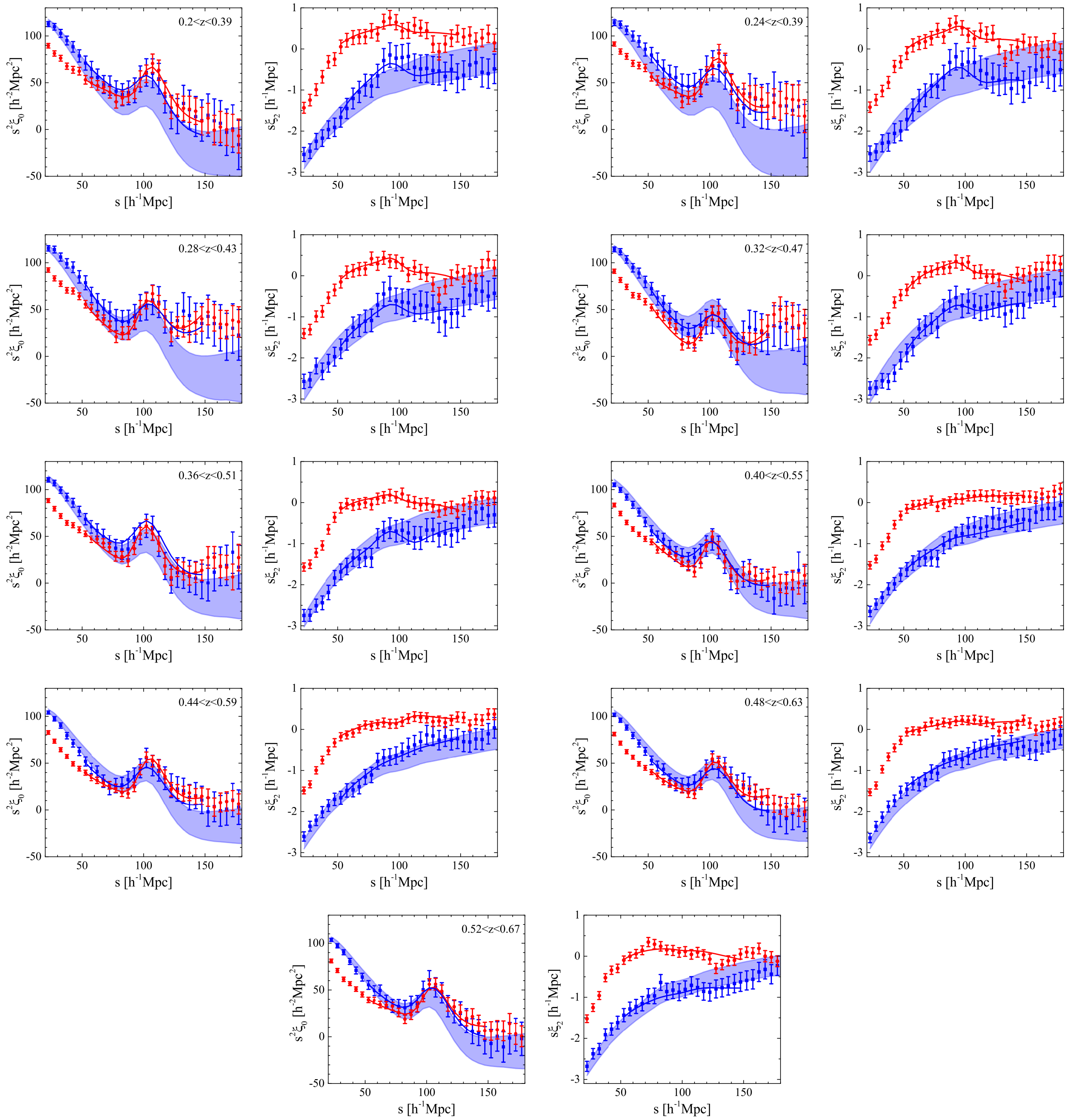

Figure 3. The measured monopole and quadrupole of correlation function in each redshift bin: in each panel the blue squares with $1\,\sigma$ error bar are the pre-reconstructed data measurements and the blue shaded regions are the average with a standard deviation of correlation function multipoles from the pre-reconstructed mocks. The red points with $1\,\sigma$ error bar are the post-reconstructed data measurements. The solid lines show the best-fit predictions from the template.

where $P^{\rm nw}(k)$ is the "no-wiggle" power spectrum, where the BAO feature is erased, which is obtained using the fitting formulae in Eisenstein & Hu (1998). The linear power spectrum $P^{\rm lin}(k)$ is calculated by CAMB[1] (Lewis et al. 2000). Σ_{nl} in the Gaussian term is a damping parameter.

Then, allowing an unknown bias factor B_ξ, which rescales the amplitude of the input template, the correlation function is given by

$$\xi^{\rm fit}(s) = B_\xi^2 \xi^{\rm mod}(\alpha s) + A^\xi(s)\,, \tag{11}$$

which includes the polynomial terms for systematics

$$A^\xi(s) = \frac{a_1}{s^2} + \frac{a_2}{s} + a_3\,. \tag{12}$$

Before doing the fitting, we normalise the model to the data at $s = 50\,h^{-1}\,{\rm Mpc}$, as done in Xu et al. (2013); Anderson et al. (2014) . While performing the fitting, we add a Gaussian prior on $\log({\rm B}_\xi^2) = 0 \pm 0.4$ (Xu et al. 2013; Anderson et al.

[1] http://camb.info

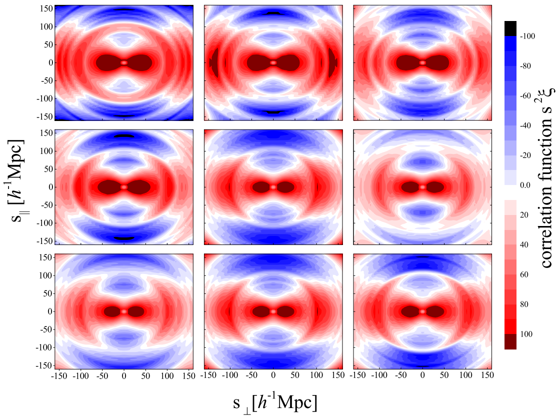

Figure 4. The 2D pre-reconstruction correlation functions in 9 redshift bins, which is assembled using the measured monopole and quadruple from the NGC and SGC samples, i.e. $\xi(s,\mu)=\xi_0(s)\mathcal{L}_0(\mu)+\xi_2(s)\mathcal{L}_2(\mu)$, here $s_\parallel=s\mu$ and $s_\perp=s\sqrt{1-\mu^2}$.

2014). So in the isotropic case, we have 5 free parameter, i.e. $[\log(B_\xi^2),\alpha,a_1,a_2,a_3]$.

The BAO feature can be measured in both the transverse and line-of-sight directions. This can be parametrised by $\alpha_\perp$ and $\alpha_{||}$, respectively

$$\alpha_\perp=\frac{D_A(z)r_d^{\rm fid}}{D_A^{\rm fid}(z)r_d}\,,\quad \alpha_\parallel=\frac{H^{\rm fid}(z)r_d^{\rm fid}}{H(z)r_d}\,. \tag{13}$$

With $\alpha_\perp$ and $\alpha_{||}$, we can define another parametrisation for the anisotropic shifts using α and a warping factor ϵ through

$$\alpha=\alpha_\perp^{2/3}\alpha_\parallel^{1/3}\,,\quad 1+\epsilon=\left(\frac{\alpha_\parallel}{\alpha_\perp}\right)^{1/3}\,. \tag{14}$$

The template for the multipoles of the correlation function in the anisotropic case is

$$\xi_\ell^{\rm mod}(s)=i^\ell\int\frac{k^2dk}{2\pi^2}P_\ell^{\rm mod}(k)j_\ell(ks), \tag{15}$$

where the the multipoles of power spectrum are

$$P_\ell^{\rm mod}(k)=\frac{2\ell+1}{2}\int_{-1}^{1}P^{\rm mod}(k,\mu)\mathcal{L}_\ell(\mu)d\mu. \tag{16}$$

The template for the 2D power spectrum is

$$P^{\rm mod}(k,\mu)=(1+\beta\mu^2)^2F(k,\mu,\Sigma_s)P_{\rm dw}^{\rm mod}(k,\mu), \tag{17}$$

where the $(1+\beta\mu^2)^2$ term corresponds to the Kaiser model for large-scale RSD (Kaiser 1987). For the reconstruction, this term is replaced by $[1+\beta\mu^2(1-S(k))]^2$ with the smoothing, $S(k)=e^{-k^2\Sigma_r^2/2}$ and $\Sigma_r=15\,h^{-1}$ Mpc (Seo et al. 2015). The term

$$F(k,\mu,\Sigma_s)=\frac{1}{(1+k^2\mu^2\Sigma_s^2)^2} \tag{18}$$

is introduced to model the small-scale FoG effect. Here the parameter Σ_s is the streaming scale and we set $4\,h^{-1}$ Mpc. The 2D de-wiggled power spectrum, compared to Eq. 10, becomes

$$\begin{aligned}P_{\rm dw}^{\rm mod}(k,\mu) &= [P_{\rm lin}(k)-P_{\rm nw}(k)]\\ &\quad\cdot\exp\left[-\frac{k^2\mu^2\Sigma_\parallel^2+k^2(1-\mu^2)\Sigma_\perp^2}{2}\right]+P_{\rm nw}(k),\end{aligned} \tag{19}$$

here the Gaussian damping term is also anisotropic. $\Sigma_\parallel$ and $\Sigma_\perp$ are the line-of-sight and transverse components of $\Sigma_{\rm nl}$, *i.e.* $\Sigma_{\rm nl}^2=(\Sigma_\parallel^2+2\Sigma_\perp^2)/3$. Here we set $\Sigma_\parallel=4\,h^{-1}$ Mpc and $\Sigma_\perp=2.5\,h^{-1}$ Mpc for the post-reconstruction and $\Sigma_\parallel=10\,h^{-1}$ Mpc and $\Sigma_\perp=6\,h^{-1}$ Mpc for the pre-reconstruction (Ross 2016).

Then the fitting models for the monopole and quadrupole of correlation function are

$$\begin{aligned}\xi_0^{\rm fit}(s) &= B_0^2\xi_0^{\rm mod}(\alpha s)+\frac{2}{5}\epsilon\left[3\xi_2^{\rm mod}(\alpha s)+\frac{d\xi_2^{\rm mod}(\alpha s)}{d\log(s)}\right]\\ &\quad+A_0(s),\end{aligned} \tag{20}$$

$$\begin{aligned}\xi_2^{\rm fit}(s) &= 2B_0^2\epsilon\frac{d\xi_0^{\rm mod}(\alpha s)}{d\log(s)}+\left(1+\frac{6}{7}\epsilon\right)\xi_2^{\rm mod}(\alpha s)\\ &\quad+\frac{4}{7}\epsilon\frac{d\xi_2^{\rm mod}(\alpha s)}{d\log(s)}+\frac{4}{7}\epsilon\left[5\xi_4^{\rm mod}(\alpha s)+\frac{d\xi_4^{\rm mod}(\alpha s)}{d\log(s)}\right]\\ &\quad+A_2(s),\end{aligned} \tag{21}$$

which are derived in Xu et al. (2013). Here a bias parameter B_0 is used to adjust the amplitude of the input template. And we include the model for systematics using the polynomial terms

$$A_\ell(s)=\frac{a_{\ell,1}}{s^2}+\frac{a_{\ell,2}}{s}+a_{\ell,3}. \tag{22}$$

As in the isotropic case, the monopole template is normalised to the measurement at $s=50\,h^{-1}$ Mpc. So in the anisotropic case, we have 10 free parameter, *i.e.* $[\alpha_\perp,\alpha_{||},\log(B_0^2),\beta,a_{\ell,1-3}]$. While performing the fitting, a Gaussian prior on $\log(B_0^2)=0\pm0.4$ is applied. We also add a Gaussian prior for the RSD parameter, *i.e.* $\beta=0.4\pm0.2$ for the pre-reconstruction and $\beta=0\pm0.2$ for the post-reconstruction (Anderson et al. 2014).

4.3 Covariance matrix

When fitting the BAO parameters, $\mathbf{p}$, we use the MCMC to search for the minimum χ^2,

$$\chi^2(\mathbf{p})\equiv\sum_{i,j}^{\ell,\ell'}\left[\xi_\ell^{th}(s_i,\mathbf{p})-\xi_\ell(s_i)\right]F_{ij}^{\ell,\ell'}\left[\xi_{\ell'}^{th}(s_j,\mathbf{p})-\xi_{\ell'}(s_j)\right].$$

where $F_{ij}^{\ell,\ell'}$ is the inverse of the covariance matrix, $C_{ij}^{\ell,\ell'}$, which is estimated using mock catalogues,

$$C_{ij}^{\ell,\ell'}=\frac{1}{N-1}\sum_k\left[\xi_\ell^k(s_i)-\bar{\xi}_\ell(s_i)\right]\left[\xi_{\ell'}^k(s_j)-\bar{\xi}_{\ell'}(s_j)\right], \tag{23}$$

where the average multipoles is given by

$$\bar{\xi}_\ell(s_i)=\frac{1}{N}\sum_k\xi_\ell^k(s_i), \tag{24}$$

here N is the number of mocks: $N=2045$ in the pre-reconstruction case and $N=1000$ in the post-reconstruction case. The unbiased estimation for the inverse covariance matrix is given by

$$\widetilde{C}_{ij}^{-1}=\frac{N-N_b-2}{N-1}C_{ij}^{-1}. \tag{25}$$

where N_b is the number of the scale bins. In order to include the error propagation from the error in the covariance matrix into the fitting parameters (Percival et al. 2014) we rescale Eq. 25 by

$$M=\sqrt{\frac{1+B(N_b-N_p)}{1+A+B(N_p+1)}} \tag{26}$$

here N_p is the number of the fitting parameters, and

$$A = \frac{2}{(N - N_b - 1)(N - N_b - 4)}, \tag{27}$$

$$B = \frac{N - N_b - 2}{(N - N_b - 1)(N - N_b - 4)}. \tag{28}$$

The normalised covariance matrix showing the correlations between monopole, quadrupole and their cross correlation in each bin is plotted in Figure 5 in the pre-reconstruction case and Figure 6 in the post-reconstruction case. From Figure 5 and Figure 6, it is seen that after reconstruction, there is less auto-correlation of multipoles and cross-correlation between multipoles.

5 TESTS ON MOCK CATALOGUES

We present the mock tests for the BAO analysis using 1000 pre-reconstructed mocks. We perform the isotropic and anisotropic BAO measurements using each individual mock catalogue in the pre-reconstruction case. The results are shown in Table 3, where $\langle\alpha\rangle$ is the average of the mean value from each mock in the isotropic case. S_α is the standard derivation of α. $\langle\sigma\rangle$ corresponds to the average of 1σ error of α fitted from each mock. The 1D distribution of the parameter α from mock tests is shown in the histogram of Figure 8. It is seen that the recovered parameter is consistent with the input cosmology. The difference between our mean result and the input cosmology is around $0.64\% - 0.81\%$.

In Table 3, $\langle\alpha_\perp\rangle$ and $\langle\alpha_\parallel\rangle$ are the average of the anisotropic BAO fitting mean value from each individual mock catalogue. $S_{\alpha_\perp}$ and $S_{\alpha_\parallel}$ are the standard derivation of the parameters $\alpha_\perp$ and $\alpha_\parallel$, respectively. $\langle\sigma_{\alpha_\perp}\rangle$ and $\langle\sigma_{\alpha_\parallel}\rangle$ correspond to the average of 1σ error of these two parameters from each individual mock catalogue. The difference of the recovered $\alpha_\perp$ value from unity is $0.15\sigma - 0.25\sigma$. For $\alpha_\parallel$, the difference is $0.17\sigma - 0.35\sigma$. But it is consistent within the uncertainty.

The BAO signals measured from the post-reconstructed mocks are more significant, as shown in the scatter plots of Figure 7, where each point in the plot corresponds to the $1\,\sigma$ error value from each pre- and post-reconstructed mock.

6 RESULTS

6.1 Isotropic BAO measurements

The correlation functions are measured with the bin width of 5 h^{-1} Mpc bins, as shown in Figure 3. We perform the fitting in the range $50 - 150\,h^{-1}$ Mpc.

We present the constraints on the isotropic BAO scale in all redshift bins in Table 4. Using the values of $D_V^{\rm fid}(z)/r_d^{\rm fid}$ for the fiducial cosmology, we derive the constraint on $D_V(z)/r_d$, as listed in the last two columns of Table 4. The measurement precision on $D_V(z)/r_d$ from the pre-reconstruction catalogue can reach $1.5\% \sim 4\%$. For the post-reconstruction, the precision is improved to be $0.9\% \sim 2.4\%$.

The improvement on the measurement precision of α after reconstruction can be seen in Figure 9, where we show our tomographic measurements in terms of the redshift in blue squares. The pre-reconstruction constraints are plotted in left panel, and the right panel shows the result after reconstruction.

In Figure 9, the green points denote the results within 3 redshift bins from $\xi(s)$ measurements in Ross (2016), *i.e.* two bins without overlapping between each other, [0.2, 0.5] and [0.5, 0.75], and an overlapping bin, [0.4, 0.6]. It is seen that with less redshift bins, more precise measurements and much tighter constraints can be obtained. In contrast, dividing more redshift bins in the tomographic case can capture the redshift information of galaxy clustering with more measurements at different effective redshifts.

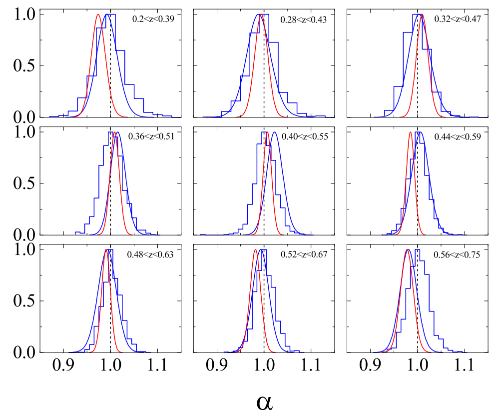

Figure 8. The 1D distribution of the parameter α from the pre-reconstructed mock catalogue (blue histograms), galaxy catalogue (blue curves) and from the post-reconstructed galaxy catalogue (red curves).

In order to test the consistency between our measurements and the measurements in 3 redshift bins (Ross 2016), we compressed our measurements into 3 redshift bins. Namely we compressed the first 4 redshift bins, which covers the redshift range from 0.2 to 0.51, into one measurement. The compression is performed by introducing a parameter and fitting it to the measurements in these 4 redshift bins with their covariance matrix. The 5th and 6th bins ($0.4 < z < 0.59$) are compressed as the second measurement value. The last compressed measurement are from the remaining bins ($0.48 < z < 0.75$). The compression results are shown in red triangles of Figure 9. We can see that within $1\,\sigma$ error, our results are consistent with the measurements in Ross (2016).

Since our redshift slices are highly correlated within the overlapping range, which is visualised in Figure 1, it is important to determine the correlations between redshift slices. We repeat the fitting on BAO parameter using each mock measurement, derive the covariance matrix between the ith z bin and jth z bin using $C_{ij} \equiv \langle\alpha_i\alpha_j\rangle - \langle\alpha_i\rangle\langle\alpha_j\rangle$, then calculate the correlation coefficient with $r_{ij} = C_{ij}/\sqrt{C_{ii}C_{jj}}$. The normalised correlations of α between redshift slices for the post-reconstruction are plotted in Figure 10. It is seen that each bin is correlated to the 3 redshift bins next to it.

6.2 Anisotropic BAO measurements

We present the fitting result on the anisotropic BAO position in Table 5 before and after reconstruction. Our measurements on $\alpha_\perp$ and $\alpha_\parallel$ are plotted in terms of redshift in blue squares of Figure 11 and 12, respectively. The green points correspond to the anisotropic BAO constraints from Ross (2016) and the red triangles are the compressed results in 3 redshift bins from our tomographic measurements. They are comparable to each other.

Based on the input fiducial values for $D_A^{\rm fid}/r_d^{\rm fid}$ and $H^{\rm fid}r_d^{\rm fid}$, we can obtain the constraints on the transverse and radial distance parameters, $D_A(z)/r_d$ and $H(z)r_d$, as listed in Table 6. The mea-

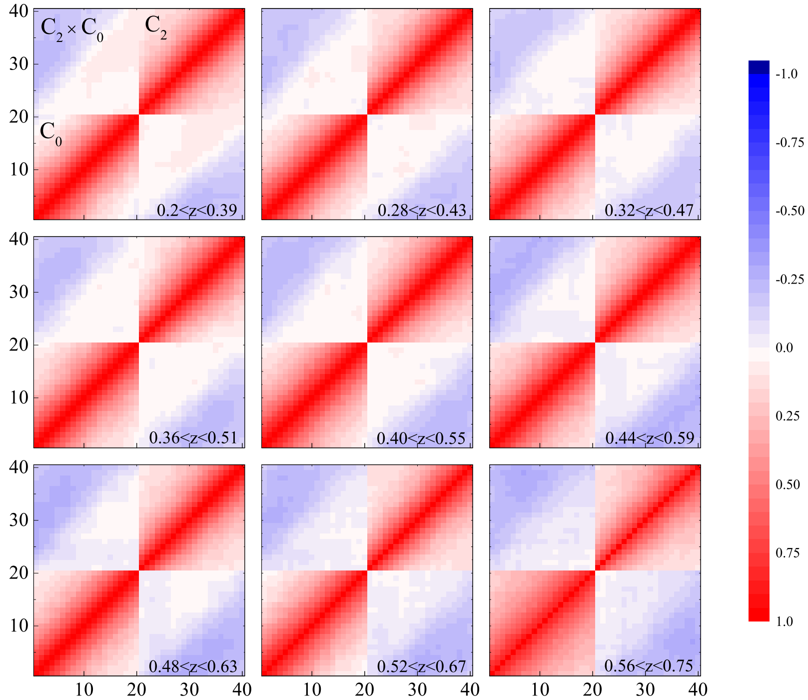

Figure 5. The correlations between monopole, C_0, quadrupole, C_2 and their cross correlation, $\mathrm{C}_0 \times \mathrm{C}_2$ for the pre-reconstruction.

Table 3. The statistics of the BAO fitting using the pre-reconstruction mocks in isotropic and anisotropic cases. $\langle\alpha\rangle$, $\langle\alpha_\perp\rangle$ and $\langle\alpha_\parallel\rangle$ are the average of the fitting mean value from each mock. S_α, $S_{\alpha_\perp}$ and $S_{\alpha_\parallel}$ are the standard derivation of the parameters α, $\alpha_\perp$ and $\alpha_\parallel$, respectively. $\langle\sigma\rangle$, $\langle\sigma_{\alpha_\perp}\rangle$ and $\langle\sigma_{\alpha_\parallel}\rangle$ correspond to the average of 1σ error of these three parameters from each mock.

$z_{\rm eff}$	$\langle\alpha\rangle$	S_α	$\langle\sigma\rangle$	$\langle\alpha_\perp\rangle$	$S_{\alpha_\perp}$	$\langle\sigma_{\alpha_\perp}\rangle$	$\langle\alpha_\parallel\rangle$	$S_{\alpha_\parallel}$	$\langle\sigma_{\alpha_\parallel}\rangle$
0.31	1.0079	0.0346	0.0318	1.0079	0.0528	0.0552	1.0158	0.0933	0.1006
0.36	1.0074	0.0319	0.0304	1.0057	0.0499	0.0518	1.0178	0.0940	0.0968
0.40	1.0081	0.0255	0.0245	1.0076	0.0427	0.0461	1.0184	0.0875	0.0877
0.44	1.0078	0.0247	0.0240	1.0067	0.0366	0.0382	1.0221	0.0795	0.0791
0.48	1.0081	0.0226	0.0212	1.0057	0.0335	0.0334	1.0246	0.0753	0.0709
0.52	1.0070	0.0208	0.0199	1.0047	0.0303	0.0311	1.0209	0.0709	0.0659
0.56	1.0071	0.0201	0.0198	1.0041	0.0302	0.0308	1.0220	0.0674	0.0646
0.59	1.0064	0.0209	0.0205	1.0053	0.0332	0.0330	1.0178	0.0691	0.0652
0.64	1.0072	0.0230	0.0225	1.0066	0.0361	0.0363	1.0183	0.0701	0.0680

Table 4. The measurement on the isotropic BAO parameters using the pre- and post-reconstruction catalogues, respectively.

$z_{\rm eff}$	pre-recon α	post-recon α	pre-recon D_V/r_d	post-recon D_V/r_d
0.31	0.9922 ± 0.0218	0.9745 ± 0.0150	8.69 ± 0.31	8.49 ± 0.12
0.36	0.9889 ± 0.0264	0.9941 ± 0.0139	9.47 ± 0.27	9.54 ± 0.14
0.40	1.0043 ± 0.0237	1.0103 ± 0.0124	10.55 ± 0.29	10.6 ± 0.13
0.44	1.0160 ± 0.0158	1.0088 ± 0.0097	11.54 ± 0.23	11.49 ± 0.11
0.48	1.0231 ± 0.0173	1.0071 ± 0.0088	12.59 ± 0.26	12.3 ± 0.11
0.52	1.0062 ± 0.0187	0.9850 ± 0.0086	13.14 ± 0.26	12.78 ± 0.11
0.56	0.9925 ± 0.0195	0.9902 ± 0.0090	13.66 ± 0.25	13.57 ± 0.13
0.59	0.9927 ± 0.0173	0.9816 ± 0.0113	14.31 ± 0.22	14.12 ± 0.16
0.64	0.9809 ± 0.0182	0.9775 ± 0.0134	14.78 ± 0.25	14.71 ± 0.21

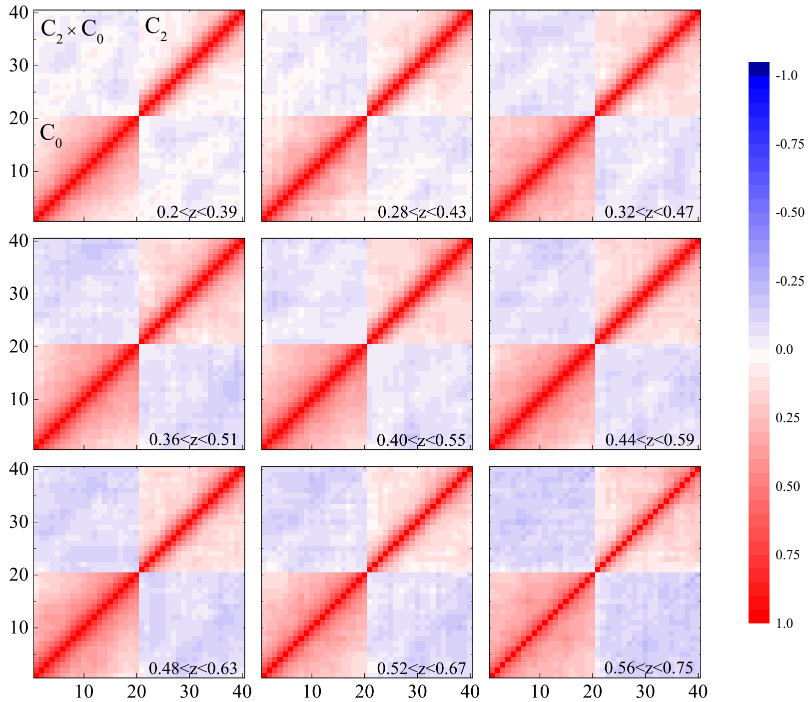

Figure 6. The correlations between monopole, C_0, quadrupole, C_2 and their cross correlation, $\mathrm{C}_0 \times \mathrm{C}_2$ for the post-reconstruction.

Table 5. The fitting results on the anisotropic BAO positions, $\alpha_\perp$ and $\alpha_\|$, using the pre- and post-reconstruction catalogues, respectively.

		pre-recon			post-recon	
$z_{\rm eff}$	$\alpha_\perp$	$\alpha_\|$	χ^2/dof	$\alpha_\perp$	$\alpha_\|$	χ^2/dof
0.31	0.9591 ± 0.0358	1.0737 ± 0.0829	$27/30$	0.9648 ± 0.0199	1.0191 ± 0.0578	$34/30$
0.36	0.9537 ± 0.0347	1.1104 ± 0.1029	$31/30$	0.9737 ± 0.0195	1.0518 ± 0.0401	$39/30$
0.4	0.9631 ± 0.0380	1.1148 ± 0.1037	$43/30$	0.9888 ± 0.0221	1.054 ± 0.0353	$40/30$
0.44	0.9705 ± 0.0267	1.1284 ± 0.0653	$36/30$	0.9999 ± 0.0171	1.0337 ± 0.0284	$33/30$
0.48	1.0130 ± 0.0322	1.0508 ± 0.0689	$40/30$	1.0078 ± 0.0159	1.0121 ± 0.0297	$42/30$
0.52	1.0140 ± 0.0264	0.9965 ± 0.0725	$42/30$	0.9945 ± 0.0136	0.9652 ± 0.024	$15/30$
0.56	1.0063 ± 0.0275	0.9676 ± 0.0640	$44/30$	0.9845 ± 0.0152	1.0029 ± 0.0254	$20/30$
0.59	0.9915 ± 0.0288	1.0002 ± 0.0515	$38/30$	0.9776 ± 0.0171	0.9832 ± 0.0305	$35/30$
0.64	0.9635 ± 0.0356	1.0151 ± 0.0544	$26/30$	0.9674 ± 0.0227	0.9972 ± 0.0337	$39/30$

Table 6. The fitting results on the anisotropic BAO distance parameters, D_A/r_d and Hr_d using the pre- and post-reconstruction catalogues, respectively.

$z_{\rm eff}$	pre-recon D_A/r_d	pre-recon $Hr_d * 10^3[\mathrm{km/s}]$	post-recon D_A/r_d	post-recon $Hr_d * 10^3[\mathrm{km/s}]$
0.31	6.30 ± 0.24	10.97 ± 0.85	6.34 ± 0.13	11.56 ± 0.66
0.36	6.93 ± 0.25	10.93 ± 1.01	7.08 ± 0.14	11.54 ± 0.44
0.40	7.47 ± 0.29	11.14 ± 1.04	7.67 ± 0.17	11.79 ± 0.39
0.44	7.98 ± 0.22	11.29 ± 0.65	8.22 ± 0.14	12.32 ± 0.34
0.48	8.73 ± 0.28	12.41 ± 0.81	8.69 ± 0.14	12.88 ± 0.38
0.52	9.09 ± 0.24	13.37 ± 0.97	8.92 ± 0.12	13.81 ± 0.34
0.56	9.33 ± 0.25	14.08 ± 0.93	9.12 ± 0.14	13.58 ± 0.34
0.59	9.47 ± 0.28	13.92 ± 0.72	9.34 ± 0.16	14.16 ± 0.44
0.64	9.51 ± 0.35	14.09 ± 0.76	9.55 ± 0.22	14.35 ± 0.48

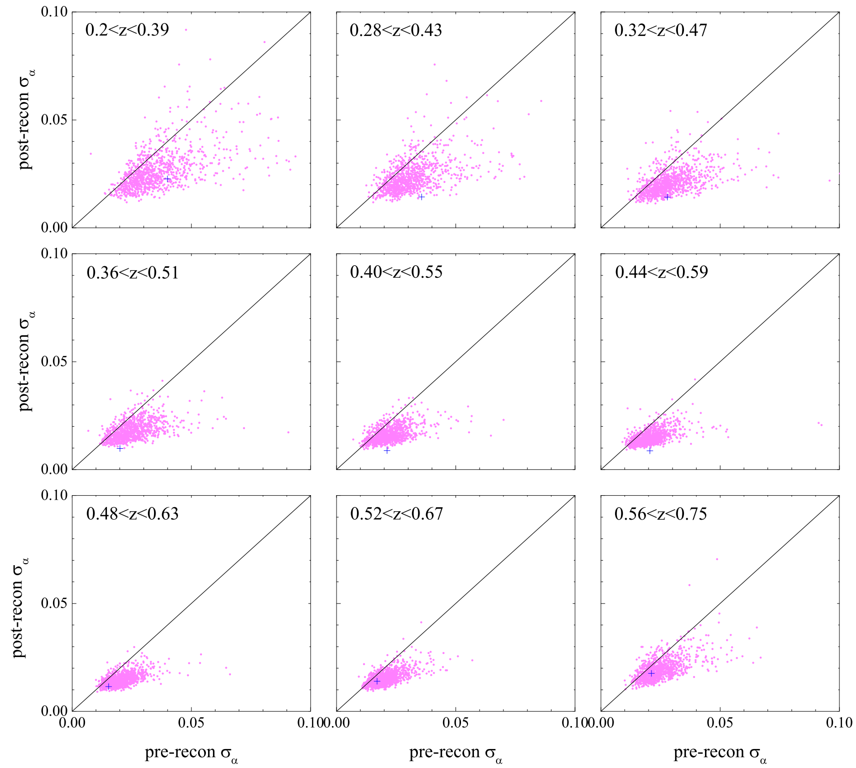

Figure 7. The scatter plot of error of α using pre- and post reconstruction mock catalogue. Each magenta point denotes the $1\,\sigma$ error of α from each mock (totally 1000 mocks) and the cross (blue) is the error measured by data.

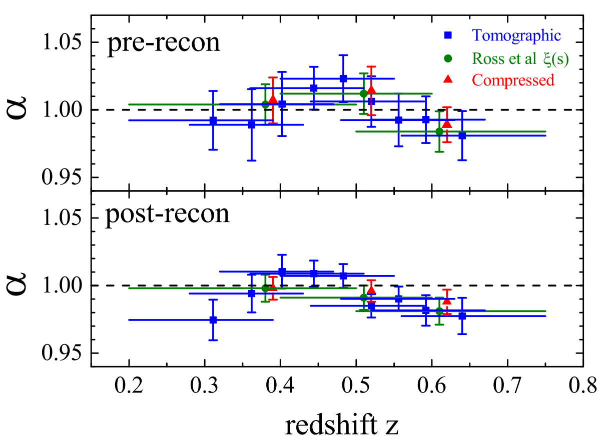

Figure 9. The fitting results on the isotropic BAO distance parameter using the pre- and post-reconstruction catalogues, respectively.

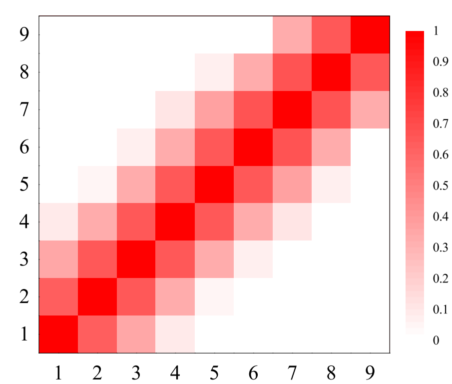

Figure 10. The normalized correlation of the parameters, α, between different redshift slices.

surement precisions are within $2.6\% - 3.9\%$ for $D_A(z)/r_d$ and $5.2\% - 9.3\%$ for $H(z)r_d$ before the reconstruction. Using the reconstructed catalogues, the precisions are improved, which can reach $1.3\% - 2.3\%$ for $D_A(z)/r_d$ and $2.5\% - 5.7\%$ for $H(z)r_d$.

We determine the correlations between overlapping redshift slices using the measurements from mock catalogue. The calculation procedure has described in Section 6.1. The normalised correlated matrix of the parameters, $\alpha_\perp$ and $\alpha_\|$, between different redshift slices for the post-reconstruction are plotted in Figure 13.

We compare our pre-reconstructed results on the isotropic and anisotropic BAO parameters with the tomographic measurements using the power spectrum in Fourier space (Zhao 2016b). The comparison is plotted in Figure 14. We can see that the isotropic results (blue points) agree well with each other. Because of the high

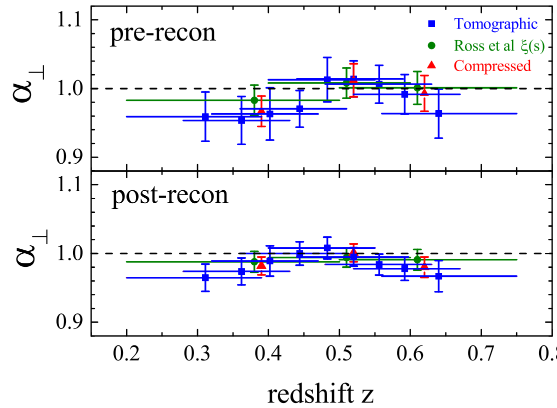

Figure 11. The fitting results on the anisotropic BAO distance parameter, $\alpha_\perp$ using the pre- and post-reconstruction catalogues, respectively.

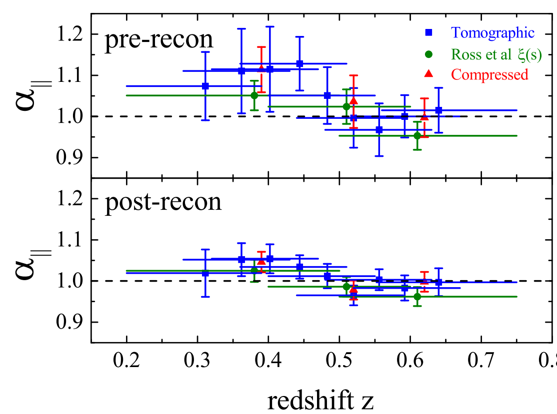

Figure 12. The fitting results on the anisotropic BAO distance parameter, $\alpha_\parallel$ using the pre- and post-reconstruction catalogues, respectively.

correlations between anisotropic parameters, the comparison looks scattered, especially for the parameter $\alpha_\parallel$. The main difference is that Zhao (2016b) use the monopole, quadrupole and hexadecapole in power spectrum, while we do not include the hexadecapole in our pre-reconstruction case. The role of the hexadecapole on anisotropic BAO constraints is discussed in detail (Zhao 2016b) .

The comparisons of our anisotropic BAO measurements with the three bins measurements in Alam (2016) are shown in Figure 15 and 16, where the black squares are our measurements, and the red points are the consensus result, which are the combined constraints from the correlation function and power spectrum in (Alam 2016). The blue bands correspond to the 68 and 95% CL constraints in the ΛCDM using the Planck data assuming a ΛCDM model (Planck Collaboration et al. 2015). We can see these results are consistent.

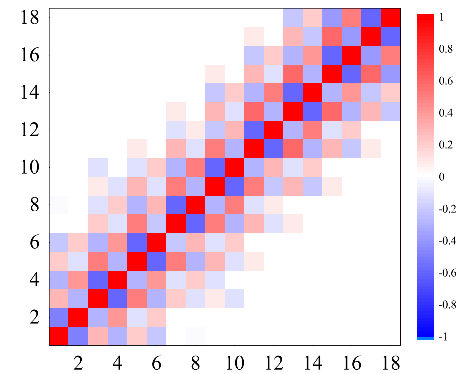

Figure 13. The normalised correlation of the parameters, $\alpha_\perp$ and $\alpha_\parallel$, between different redshift slices.

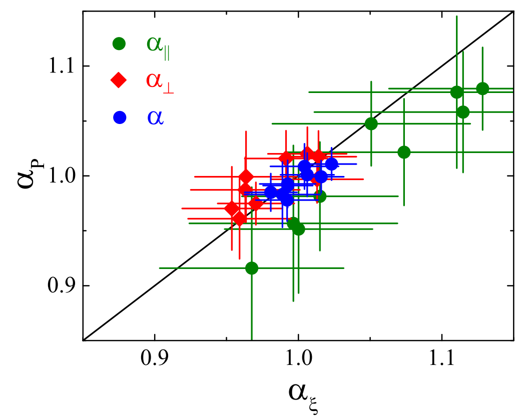

Figure 14. The comparison of our result on isotropic and anisotropic BAO parameters with that in Zhao (2016b) measured in Fourier space.

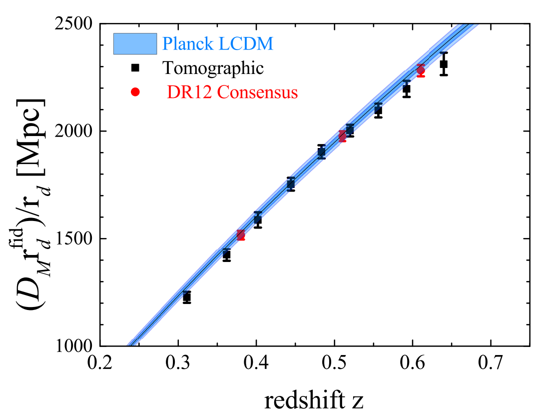

Figure 15. Our tomographic measurements on $D_M r_d^{\rm fid}/r_d$ (black squares) in terms of redshift, compared with the consensus result (red points) in Alam (2016) and the prediction from Planck assuming a ΛCDM model (blue bands).

7 CONSTRAINTS ON COSMOLOGICAL MODELS

Using our tomographic measurements on Hubble parameters, we do the Om diagnostic, proposed by Sahni et al. (2008). It is defined

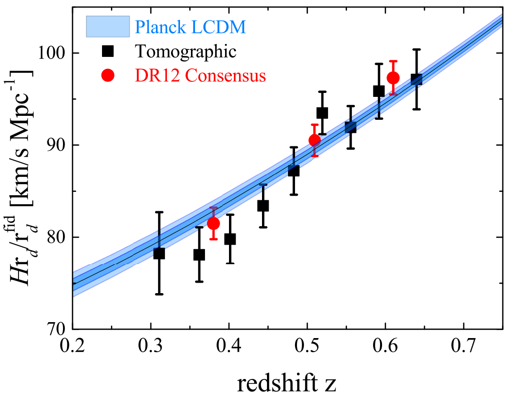

Figure 16. Our tomographic measurements on $H(z)r_d/r_d^{\rm fid}$ (black squares) in terms of redshift, compared with the consensus result (red points) in Alam (2016) and the prediction from Planck assuming a ΛCDM model (blue bands).

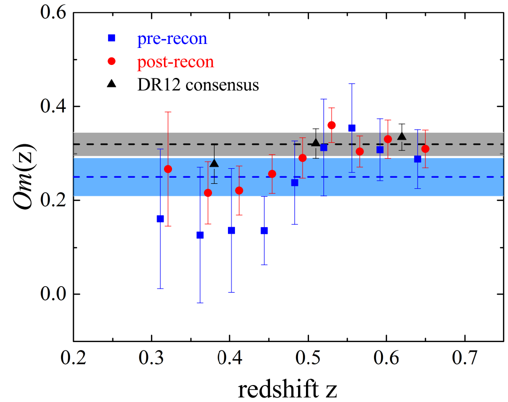

Figure 17. The $Om(z)$ values converted by our measurements on Hubble parameter in 9 redshift bins.

by the Hubble parameter

$$Om(z) \equiv \frac{[H(z)/H_0]^2 - 1}{(1+z)^3 - 1}. \tag{29}$$

In ΛCDM, $Om(z) = \Omega_m$. Using our measurements of $H(z)r_d$ and combining the constraint on r_d from Planck results (Planck Collaboration et al. 2014), we convert our measurements to $Om(z)$, as shown in Figure 17, where the blue squares are the pre-reconstruction tomographic measurements, the red points are the post-reconstruction tomographic measurements, and the black triangles are the consensus result in Alam (2016). To quantify the possible deviation from ΛCDM, we make a fit to the $Om(z)$ values with the covariance matrix between different redshift slices using one parameter. As shown in Figure 17, the black dashed line with the grey band are the best-fit value with $1\,\sigma$ error using the "3 $z$bin" consensus result, and the blue dashed line with the blue band are the "9 $z$bin" pre-reconstruction tomographic result. The values of χ^2 are less than 4. Therefore, within $2\,\sigma$ regions there is no deviation from a constant Ω_m.

We present the cosmological implications with our tomographic BAO measurements. We use the Cosmomc[2] (Lewis & Bridle 2002) code to perform the fittings on cosmological parameters in the flat ΛCDM and a time-varying dark energy with EoS, $w(a) = w_0 + w_a(1-a)$ (Chevallier & Polarski 2001; Linder 2003).

We are using the combined data set, including the temperature and polarization power spectra from Planck 2015 data release (Planck Collaboration et al. 2015), the "Joint Light-curve Analysis" (JLA) sample of type Ia SNe (Sako et al. 2014), the BOSS DR12 BAO distance measurements. We compare the constraining power of different BAO measurements, *i.e.* tomographic "9 $z$bin" BAO measurements from the post-reconstructed catalogues, consensus "3 $z$bin" measurements on BAO and RSD in Alam (2016), and the compressed "1 $z$bin" BAO result from the post-reconstruction tomographic measurements.

The results of the parameters Ω_m, H_0, w_0 and w_a are presented in Table 7. We can see the uncertainties of parameters are improved with the "9 $z$bin" BAO measurements in our work.

[2] http://cosmologist.info/cosmomc/

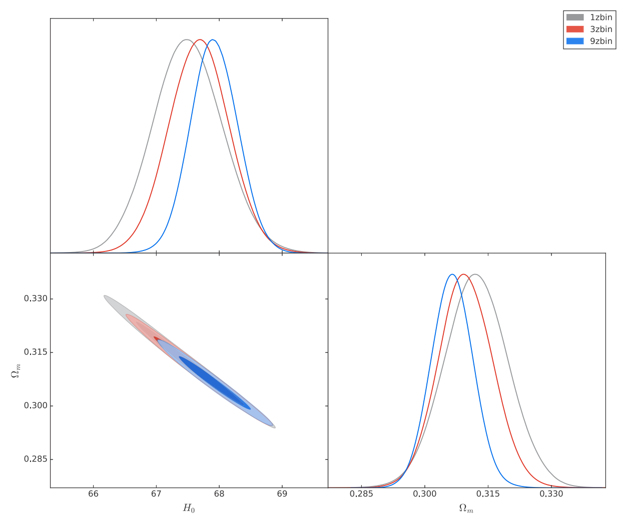

Figure 18. The1D posterior distribution of Ω_m and H_0 and their 2D contour plots in the ΛCDM from the compressed "1 $z$bin" BAO (grey line and contour), consensus "3 $z$bin" BAO and RSD (red line and contour), and tomographic "9 $z$bin" BAO (blue line and contour).

The constraint precisions of the parameters, Ω_m and H_0 in ΛCDM, are improved by 55% and 47%, respectively, compared the tomographic "9 $z$bin" with compressed "1 $z$bin" results. Comparing the "9 $z$bin" with "3 $z$bin" results, the errors of Ω_m and H_0 are improved by 33% and 26%, respectively. Figure 18) shows the 1D posterior distribution of Ω_m and H_0 and their 2D contour plots from the compressed "1 $z$bin" BAO (grey line and contour), consensus "3 $z$bin" BAO and RSD (red line and contour), and tomographic "9 $z$bin" BAO (blue line and contour).

In w_0w_aCDM, comparing the tomographic "9 $z$bin" with compressed "1 $z$bin" results, the errors of w_0 and w_a are improved by 11% and 45%, respectively. Using the Figure of Merit (FoM) (Albrecht et al. 2009), which is inversely proportional to the area of the contour as shown in Figure 19, to quantify this improvement, the FoM is improved by a factor of 1.35 (FoM=43 for the grey contour from the "1 $z$bin" result and FoM=67 for the blue contour from the "9 $z$bin" result in Figure 19). Comparing the "9 $z$bin" with "3 $z$bin" results, the errors of w_0 and w_a are slightly improved by 4%.

Table 7. Joint data constraints on the cosmological parameters Ω_m, H_0 and dark energy EoS parameters w_0 and w_a in the ΛCDM and w_0w_aCDM. Here we compare the constraining power of the BOSS DR12 BAO measurements, i.e. the tomographic "9 $z$bin" measurements in this work, consensus "3 $z$bin" measurements in Alam (2016), and the compressed "1 $z$bin" result from tomographic measurements.

Model	Joint Data set Planck+JLA+BOSS	Ω_m	H_0	w_0	w_a
ΛCDM	Tomographic (9 $z$bin)	0.3065 ± 0.0049	67.92 ± 0.38	-1	-
ΛCDM	DR12 Consensus (3 $z$bin)	0.3098 ± 0.0065	67.68 ± 0.48	-1	-
ΛCDM	Compressed (1 $z$bin)	0.3122 ± 0.0076	67.50 ± 0.56	-1	-
w_0w_aCDM	Tomographic (9 $z$bin)	0.3031 ± 0.0090	68.69 ± 1.01	-0.9795 ± 0.0926	-0.2897 ± 0.3352
w_0w_aCDM	DR12 Consensus (3 $z$bin)	0.3099 ± 0.0094	67.79 ± 0.98	-0.9610 ± 0.0966	-0.2011 ± 0.3491
w_0w_aCDM	Compressed (1 $z$bins)	0.3024 ± 0.0115	68.83 ± 1.28	-0.9609 ± 0.1096	-0.4006 ± 0.4856

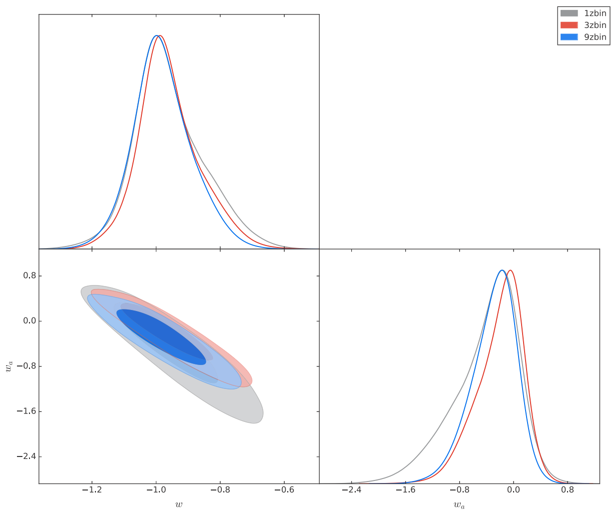

Figure 19. The 1D posterior distribution of w and w_a and their 2D contour plots in the CPL model from the compressed "1 $z$bin" BAO (grey line and contour), consensus "3 $z$bin" BAO and RSD (red line and contour), and tomographic "9 $z$bin" BAO (blue line and contour).

8 CONCLUSION

Measurements of the BAO distance scales have become a robust way to map the expansion history of the Universe. A precise BAO distance measurement at a single effective redshift can be achieved using the entire galaxies in the survey, covering a wide redshift range. However, the tomographic information is largely lost. To extract the redshift information from the samples, one possible way is to use overlapping redshift slices.

Using the combined sample of BOSS DR12, we perform a tomographic baryon acoustic oscillations analysis using the two-point galaxy correlation function. We split the whole redshift range of sample, $0.2 < z < 0.75$, into multiple overlapping redshift slices, and measured correlation functions in all the bins. With the full covariance matrix calibrated using MultiDark-Patchy mock catalogues, we obtained the isotropic and anisotropic BAO measurements.

In the isotropic case, the measurement precision on $D_V(z)/r_d$ from the pre-reconstruction catalogue can reach $1.5\% \sim 4\%$. For the post-reconstruction, the precision is improved, and becomes $0.9\% \sim 2.4\%$. In the anisotropic case, the measurement precision is within $2.6\% - 3.9\%$ for $D_A(z)/r_d$ and $5.2\% - 9.3\%$ for $H(z)r_d$ before the reconstruction. Using the reconstructed catalogues, the precision is improved, which can reach $1.3\% - 2.3\%$ for $D_A(z)/r_d$ and $2.5\% - 5.7\%$ for $H(z)r_d$.

We present the comparison of our measurements with that in a companion paper (Zhao 2016b), where the tomographic BAOs is measured using multipole power spectrum in Fourier space. We find an agreement within the $1\,\sigma$ confidence level. The derived 3-bin results from our tomographic measurements are also compared to the 3-bin measurements in Ross (2016), and a consistency is found.

We perform cosmological constraints using the tomographic 9-bin BAO measurements, the consensus 3-bin BAO and RSD measurements, and the compressed 1-bin BAO measurement. Comparing the 9-bin and 1-bin BAO distance measurements, the uncertainties of the parameters, Ω_m and H_0 in ΛCDM, are improved by 55% and 47%, respectively. For w_0w_aCDM, the FoM is improved by a factor of 1.35. Comparing the 9-bin and 3-bin measurements, the uncertainties of the parameters, Ω_m and H_0 in ΛCDM, are improved by 33% and 26%, respectively. For w_0w_aCDM, the errors of w_0 and w_a are slightly improved by 4%.

The future galaxy surveys will cover a larger and larger cosmic volume, and there is rich tomographic information in redshifts to be extracted. The method developed in this work can be easily applied to the upcoming galaxy surveys and the gain in the temporal information is expected to be more significant.

ACKNOWLEDGEMENTS

YW is supported by the NSFC grant No. 11403034. GBZ and YW are supported by the Strategic Priority Research Program "The Emergence of Cosmological Structures" of the Chinese Academy of Sciences Grant No. XDB09000000, by National Astronomical Observatories, Chinese Academy of Sciences, and by University of Portsmouth.

Funding for SDSS-III has been provided by the Alfred P. Sloan Foundation, the Participating Institutions, the National Science Foundation, and the US Department of Energy Office of Science. The SDSS-III web site is http://www.sdss3.org/. SDSS-III is managed by the Astrophysical Research Consortium for the Participating Institutions of the SDSS-III Collaboration including the University of Arizona, the Brazilian Participation Group, Brookhaven National Laboratory, Carnegie Mellon University, University of Florida, the French Participation Group, the German Participation Group, Harvard University, the Instituto de Astrofisica de Canarias, the Michigan State/Notre Dame/JINA Participation Group, Johns Hopkins University, Lawrence Berkeley

National Laboratory, Max Planck Institute for Astrophysics, Max Planck Institute for Extraterrestrial Physics, New Mexico State University, New York University, Ohio State University, Pennsylvania State University, University of Portsmouth, Princeton University, the Spanish Participation Group, University of Tokyo, University of Utah, Vanderbilt University, University of Virginia, University of Washington, and Yale University.

This research used resources of the National Energy Research Scientific Computing Center, which is supported by the Office of Science of the U.S. Department of Energy under Contract No. DE-AC02-05CH11231, the SCIAMA cluster supported by University of Portsmouth, and the ZEN cluster supported by NAOC.

REFERENCES

Alam S. e. a., 2016. Submitted
Alam S., et al., 2015, ApJS, 219, 12
Albrecht A., et al., 2009, preprint, (arXiv:0901.0721)
Anderson L., et al., 2014, MNRAS, 441, 24
Beutler F. e. a., 2016a. Submitted
Beutler F. e. a., 2016b. Submitted
Beutler F., et al., 2011, MNRAS, 416, 3017
Blake C., et al., 2011, MNRAS, 418, 1707
Chevallier M., Polarski D., 2001, International Journal of Modern Physics D, 10, 213
Chuang C.-H. e. a., 2016. Submitted
Chuang C.-H., Wang Y., 2012, MNRAS, 426, 226
Chuang C.-H., Wang Y., 2013, MNRAS, 431, 2634
Cuesta A. J., et al., 2016, MNRAS, 457, 1770
Dawson K. S., et al., 2013, AJ, 145, 10
Eisenstein D. J., Hu W., 1998, ApJ, 496, 605
Eisenstein D. J., et al., 2005, ApJ, 633, 560
Eisenstein D. J., Seo H.-J., White M., 2007a, ApJ, 664, 660
Eisenstein D. J., Seo H.-J., White M., 2007b, ApJ, 664, 660
Eisenstein D. J., et al., 2011, AJ, 142, 72
Feldman H. A., Kaiser N., Peacock J. A., 1994, ApJ, 426, 23
Gil-Marín H., et al., 2015, preprint, (arXiv:1509.06373)
Grieb J. N. e. a., 2016. Submitted
Kaiser N., 1987, MNRAS, 227, 1
Kazin E. A., et al., 2010, ApJ, 710, 1444
Kazin E. A., Sánchez A. G., Blanton M. R., 2012, MNRAS, 419, 3223
Kazin E. A., et al., 2013, MNRAS, 435, 64
Kitaura F.-S., et al., 2016, MNRAS, 456, 4156
Landy S. D., Szalay A. S., 1993, ApJ, 412, 64
Lewis A., Bridle S., 2002, Phys. Rev. D, 66, 103511
Lewis A., Challinor A., Lasenby A., 2000, ApJ, 538, 473
Linder E. V., 2003, Physical Review Letters, 90, 091301
Padmanabhan N., White M., 2008, Phys. Rev. D, 77, 123540
Padmanabhan N., Xu X., Eisenstein D. J., Scalzo R., Cuesta A. J., Mehta K. T., Kazin E., 2012, MNRAS, 427, 2132
Pellejero-Ibanez M. e. a., 2016. Submitted
Percival W. J., Cole S., Eisenstein D. J., Nichol R. C., Peacock J. A., Pope A. C., Szalay A. S., 2007, MNRAS, 381, 1053
Percival W. J., et al., 2014, MNRAS, 439, 2531
Perlmutter S., et al., 1999, ApJ, 517, 565
Planck Collaboration et al., 2014, A&A, 571, A16
Planck Collaboration et al., 2015, preprint, (arXiv:1507.02704)
Reid B. A., et al., 2010, MNRAS, 404, 60
Riess A. G., et al., 1998, AJ, 116, 1009
Ross A. J. e. a., 2016. Submitted
Sahni V., Shafieloo A., Starobinsky A. A., 2008, Phys. Rev. D, 78, 103502
Sako M., et al., 2014, preprint, (arXiv:1401.3317)
Salazar-Albornoz S. e. a., 2016. Submitted
Salazar-Albornoz S., Sánchez A. G., Padilla N. D., Baugh C. M., 2014, MNRAS, 443, 3612
Sánchez A. G. e. a., 2016a. Submitted
Sánchez A. G. e. a., 2016b. Submitted
Seo H.-J., Eisenstein D. J., 2007, ApJ, 665, 14
Seo H.-J., Beutler F., Ross A. J., Saito S., 2015, preprint, (arXiv:1511.00663)
Tegmark M., 1997, Physical Review Letters, 79, 3806
Tegmark M., et al., 2006, Phys. Rev. D, 74, 123507
Vargas-Magaña M., et al., 2016. Submitted
Weinberg D. H., Mortonson M. J., Eisenstein D. J., Hirata C., Riess A. G., Rozo E., 2013, Phys. Rep., 530, 87
Xu X., Cuesta A. J., Padmanabhan N., Eisenstein D. J., McBride C. K., 2013, MNRAS, 431, 2834
Zhao G.-B. e. a., 2016a. In preparation
Zhao G.-B. e. a., 2016b. Submitted